

1 **EXPERIMENTAL ANALYSIS OF STEEL BEAMS SUBJECTED TO FIRE ENHANCED BY BRILLOUIN**
2 **SCATTERING BASED FIBER OPTIC SENSOR DATA**

3 Yi Bao¹, S.M.ASCE, Yizheng Chen², Matthew S. Hoehler³, M.ASCE, Christopher M. Smith⁴,
4 M.ASCE, Matthew Bundy⁵, and Genda Chen⁶, F.ASCE

5 **ABSTRACT**

6 This paper presents high temperature measurements using a Brillouin scattering based fiber
7 optic sensor and the application of the measured temperatures and building code recommended
8 material parameters into enhanced thermo-mechanical analysis of simply-supported steel beams
9 subjected to combined thermal and mechanical loading. The distributed temperature sensor
10 captures detailed, non-uniform temperature distributions that are compared locally with
11 thermocouple measurements with less than 4.7% average difference at 95% confidence level.
12 The simulated strains and deflections are validated using measurements from a second
13 distributed fiber optic (strain) sensor and two linear potentiometers, respectively. The results
14 demonstrate that the temperature-dependent material properties specified in the four investigated
15 building codes lead to strain predictions with less than 13% average error at 95% confidence
16 level, and that the EN1993-1-2 building code provided the best predictions. However, the
17 implicit consideration of creep in the EN1993-1-2 is insufficient when the beam temperature
18 exceeds 800°C.

19 **Keywords:** Steel beams; Thermo-mechanical analysis; Non-uniform temperature distribution;
20 Distributed fiber optic sensors; Fire.

¹Ph.D. Candidate, Missouri University of Science and Technology, Rolla, MO 65409.

²Ph.D. Candidate, Missouri University of Science and Technology, Rolla, MO 65409.

³Research Structural Engineer, National Institute of Standards and Technology, Gaithersburg, MD 20899.

⁴Research Structural Engineer, National Institute of Standards and Technology, Gaithersburg, MD 20899.

⁵Director, National Fire Research Laboratory, National Institute of Standards and Technology, Gaithersburg, MD 20899.

⁶(Corresponding author), Professor and Abbett Distinguished Chair in Civil Engineering, Missouri University of Science and Technology, Rolla, MO 65409. Email: gchen@mst.edu, Phone: (573)341-4462, Fax: (573)341-4729.

21 **INTRODUCTION**

22 When a steel structural component is subjected to elevated temperatures, both its material
23 properties and geometry change. The Young's modulus and yield strength of steel degrade
24 quickly with increasing temperature for temperatures greater than 400°C (Usmani *et al.* 2003).
25 The degradation of mechanical properties directly reduces the load carrying capacity of a
26 structure. Additionally, thermal expansion can cause changes in connection conditions leading to
27 structural instability and collapse (Sunder 2005). Restraint of thermal expansion can result in
28 large stresses that can cause buckling or yielding of structural members. Therefore, thermal
29 effects can substantially influence the performance of steel structures in fire (Huang and Tan
30 2003; Tan *et al.* 2007).

31 To improve the safety of buildings in a fire, extensive experimental investigations of large-
32 scale steel structures have been carried out in the past. Typical measurements in these
33 investigations included temperature, strain, displacement, and load. With the exception of
34 temperature, almost all measurements were obtained from locations outside of the heated zone.
35 For example, Tan *et al.* (2007) and Dwaikat *et al.* (2011) investigated the behavior of steel
36 columns in a furnace with displacements and loads measured using transducers placed outside of
37 the heated zone. Dwaikat *et al.* (2011) applied strain gauges to a section of each steel test
38 specimen located outside of a test furnace to measure localized strains. Li and Guo (2008)
39 subjected steel beams to heating in fire and subsequent cooling and measured loads and
40 deformations outside of the high-temperature zone. Strain gauges were installed on auxiliary
41 members to indirectly determine forces based on force equilibrium. High-temperature resistance-
42 based strain gauges have been reported to be unreliable in structural applications with fire
43 (McAllister *et al.* 2012).

44 Fiber Bragg grating (FBG) sensors were used by Zhang and Kahrizi (2007) to measure strain
45 and temperature; however, the sensors began to degrade when heated over 300°C and the fiber
46 gratings were erased completely around 600°C. Similarly, Huang *et al.* (2010) used long period
47 fiber grating sensors inscribed in optical fibers for strain and temperature measurement up to
48 700°C. Both types of gratings had limited thermal stability for fire applications (Venugopalan
49 2010; Huang *et al.* 2013). Regenerated FBG sensors with enhanced thermal stability were used
50 to successfully monitor temperature changes in fire by Rinaudo *et al.* (2015). Nevertheless,
51 grating sensors provide measurements only at discrete points. Therefore, fully-distributed fiber
52 optic sensors that utilize Brillouin optical time domain analysis (BOTDA) or Brillouin optical
53 time domain reflectometer (BOTDR) technology (Bao and Chen 2011) and provide multiple
54 measurements along a fiber have recently attracted attention in the research community. The
55 application of BOTDR and BOTDA, however, is limited due to low spatial resolution of the
56 measurements, often as large as 15 cm (Bao and Chen 2011). Recently, a pulse pre-pumped
57 BOTDA (PPP-BOTDA) technology has been commercialized for simultaneous strain and
58 temperature measurement with 2 cm spatial resolution over a measurement distance of 0.5 km
59 (Kishida and Li 2006; Bao *et al.* 2015). However, implementation of distributed fiber optic
60 sensors for structural fire research has not been fully explored.

61 Based on experimental investigations, analytical (Usmani *et al.* 2001; Huang and Tan 2003)
62 and numerical (Choi 2008; Zhang *et al.* 2012, 2013) studies were carried out, and various
63 computational models were proposed to predict the thermal and mechanical responses of steel
64 beams and columns in fire, including the spatial and temporal temperature distributions and
65 structural deflections.

66 Thermo-mechanical analysis procedures for structures or structural components in the

67 literature can be categorized as sequentially-coupled or fully-coupled. When the thermal
68 responses can be considered independent of the mechanical responses, a sequentially-coupled
69 thermo-mechanical analysis (Jeffers and Sotelino 2012) can be performed. In this case, thermo-
70 dynamic and heat transfer analyses are first conducted to predict the temperature distributions.
71 Then, the predicted temperature distributions are applied to determine the thermal expansion and
72 temperature-dependent material properties. Finally, mechanical analysis is carried out to predict
73 the structural performance.

74 When the mechanical response can significantly influence the thermal response, a fully-
75 coupled thermo-mechanical analysis must be performed. In a fully-coupled analysis, the
76 incremental results of the structural model are used to incrementally update the boundary
77 conditions in the thermo-dynamic model.

78 Both sequentially-coupled and fully-coupled thermo-mechanical analysis require the
79 prediction of temperature distributions. Even though zone models (Cadorin and Franssen 2003;
80 Li and Zhang 2012), computational fluid dynamics models; e.g. the Fire Dynamics Simulator
81 (McGrattan *et al.* 2010), and stochastic models (Bertola and Cafaro 2009) for fire have been
82 developed, it is difficult to accurately predict the resulting temperature distributions. The error in
83 the predicted temperature distribution can result in inaccurate mechanical response of the
84 structure. Most importantly, the error in temperature distribution and the inaccuracy in
85 mechanical response cannot be quantified without properly measured data, which is difficult to
86 obtain when test objects and sensors are engulfed in flames.

87 In this study, we directly measure temperatures using a distributed fiber optic temperature
88 sensor under fire conditions. The measured temperature distributions are then applied for
89 enhanced thermal-mechanical analysis of steel beams under combined fire and static loading to

90 assess building code-specified relations for temperature-dependent mechanical properties of the
91 steel. The measured temperatures from the distributed temperature sensor are compared to results
92 obtained using thermocouples. The simulated strains and deflections from the structural analysis
93 are validated using a distributed strain sensor that uses Brillouin scattering and two linear
94 potentiometers, respectively.

95 **EXPERIMENTAL PROGRAM**

96 **Test Specimen and Setup**

97 Three S3×5.7 ASTM A36 low carbon steel “I-shaped” sections (AISC 2011), designated as
98 Beam #1, #2, and #3, were tested under three-point loading in a reconfigurable compartment fire
99 setup (“flame channel”) as shown in Figs. 1(a-c). Each beam was 76 mm deep, 59 mm wide, and
100 1420 mm long. The cross-sectional area and moment of inertia about the strong axis were 1,077
101 mm² and 10⁶ mm⁴, respectively.

102 The flame channel, which was located under a 6 m × 6 m (plan) exhaust hood, included three
103 subassemblies: a burner rack, an enclosure, and a specimen loading system. The burner rack (Fig.
104 1(b)) had four independent natural gas diffusion burners made of sheet metal 300 mm × 300 mm
105 × 140 mm (length × width × height) in dimension. After the natural gas entered a burner from the
106 bottom, it filled the burner cavity and passed through a 20 mm thick ceramic fiber blanket to
107 distribute the gas. The burners were manually regulated using a needle valve on the gas line, and
108 the energy content of the supplied gas was measured with an expanded uncertainty of less than
109 2.4% (Bundy *et al.* 2007).

110 An enclosure constructed of square tube steel, cold-formed steel C-profiles and gypsum
111 board lined with thermal ceramic fiber enclosed the space above the burner rack. The enclosure
112 was open at three faces: the bottom and the two ends in longitudinal direction of the beam,

113 creating the compartment flame dynamics depicted in Fig. 1(c). The heated “compartment”
114 created by the enclosure was approximately 380 mm × 400 mm × 1830 mm (height × width ×
115 length) in size and reduced radiative heat losses.

116 Each beam was simply supported at a clear-span of 1250 mm on two supports constructed of
117 1-1/2” Schedule 40 pipe (outer diameter: 48 mm), which were supported on concrete blocks. The
118 specimen was loaded by a U-shape 1/2” Schedule 40 pipe (outer diameter: 21 mm) “loading
119 yoke” at the mid-span (Fig. 1(a)). Both the supporting and the loading pipes were water-cooled
120 with the exiting water temperature controlled to less than 50°C, which limited undesired thermal
121 movement of the boundary conditions. Load was transferred to the yoke with the pulley system
122 depicted in Figs. 1(a) and 1(c).

123 **Instrumentation**

124 Data from the fuel delivery system, thermocouples, displacement sensors and a load
125 transducer were measured continuously using a National Instruments data acquisition system (NI
126 PXIe-1082). Thermocouple data were recorded using 24-bit Thermocouple Input Modules (NI
127 PXIe-4353), and load and displacement data were recorded using a high-speed, 16-bit
128 multifunction module (NI PXIe-6363). Data were sampled at 90 Hz with average values and
129 standard deviations recorded in the output file at a rate of 1 Hz.

130 A Neubrescope data acquisition system (NBX-7020) for the distributed fiber optic sensors
131 was used to perform PPP-BOTDA measurements (Kishida and Li 2006; Bao and Chen 2015,
132 2016a). Using a pulse bandwidth of 0.2 ns, 2 cm spatial resolution was obtainable with
133 accuracies of 0.75°C and 15 µε for temperature and strain at an average count of 2¹⁴ (Neubrex
134 2013). In this test, the sampling and spatial resolutions were set at 1 cm and 2 cm, respectively,
135 meaning that data points were sampled at every 1 cm and the Brillouin frequency shifts of two

136 points spaced at no less than 2 cm could be distinguished. The measurement distance was set to
137 50 m. The scanning frequency ranged from 10.82 GHz to 11.67 GHz, which approximately
138 corresponded to a target temperature range from 20°C to 1100°C (Bao and Chen 2015). The
139 reading time varied from 15 seconds to 40 seconds depending on the scanning frequency range.

140 *Distributed Fiber Optic Sensors (DFOSs)*

141 Two single-mode optical fibers with dual-layer coating were used as a distributed
142 temperature sensor (DFOS-T) and a distributed temperature and strain sensor (DFOS-ST) with
143 the PPP-BOTDA, respectively. The single-mode fiber had a glass core (diameter: 8.2 μm), a
144 glass cladding (outer diameter: 125 μm), a soft inner coating (outer diameter: 190 μm), and a
145 stiff outer coating (outer diameter: 242 μm). The soft and stiff layers protect the glass from
146 mechanical impact and from abrasion and environmental exposure, respectively. Both layers are
147 composed of monomers, oligomers, photoinitiators, and additives (Kouzmina *et al.* 2010). The
148 distributed sensors measure Brillouin frequency shifts due to temperature and/or strain changes
149 (Bao *et al.* 2015). Once calibrated, the sensors can be used to evaluate the temperature and strain
150 changes from the measured Brillouin frequency shifts (Bao and Chen 2015, 2016b).

151 For strain measurement, the coatings must be removed before the optical fiber is attached to a
152 specimen to ensure effective strain transfer at high temperature. Figs. 2(a) and 2(b) show the
153 schematic and prototype of a strain sensor package. The bare optical fiber was passed through
154 two glass tubes (Glass tube 1 in Fig. 2) in series with a small gap between them, and fixed to the
155 tubes at their far ends using a two-part high-temperature adhesive. The gap between the two
156 tubes was covered with a third tube (Glass tube 2 in Fig. 2) for additional protection of the fiber.
157 Each Glass tube 1 was fixed near the gap on the steel beam with a clip and laterally constrained
158 at the far end with a ring. The leg of each ring or clip was tightly inserted into a small hole (\approx

159 1.4 mm in diameter) pre-drilled on the steel beam. When installed, the two rings and the two
160 clips were aligned using a steel guide bar as depicted in Fig. 2(b).

161 The strain sensor measures the elongation of steel between the two clips over a base length
162 denoted by d . To enable large strain measurements, the steel elongation is averaged over a gage
163 length of the sensor, denoted by L . A gage length factor α of the sensor can thus be defined as the
164 ratio of the gage length and the base length, or $\alpha = L/d$ (Huang *et al.* 2010). Since the optical
165 fiber has limited strain capacity before rupture, increasing α allows for an increased strain
166 measurement range, but leads to reduced sensitivity and spatial resolution. In this study, α was
167 designed to be 10, providing a maximum strain capacity of approximately 10000 $\mu\epsilon$ (1%). As
168 shown in Fig. 2(a), the optical fiber for strain sensing had a stand-off distance of 2.5 ± 0.5 mm
169 from the surface of the specimen.

170 For temperature measurement, the coatings of the optical fiber were left in place to provide
171 protection during installation. The protective coatings burn off at 300°C – 400°C with negligible
172 influence on the temperature measurement, while the glass core and cladding can survive to
173 temperatures above 1000°C.

174 Each beam was instrumented with three strain-temperature sensors as shown in Fig. 3:
175 DFOS-ST1 and DFOS-ST2 on the bottom flange at mid-span and quarter-span of the beam,
176 respectively, and DFOS-ST3 on the top flange at quarter-span. The optical fiber as a light
177 transmission cable of DFOS-ST1, DFOS-ST2, and DFOS-ST3 or as a distributed temperature
178 sensor (DFOS-T in Fig. 3) was passed along the top and bottom flanges of each beam to form a
179 closed loop with the Neubrescope for PPP-BOTDA measurements. It was intermittently and
180 loosely attached to the surface of the beam using a two-part high temperature adhesive. The
181 transmission cable and the temperature sensor were closely spaced, and thus subjected to

182 approximately the same temperatures. Therefore, the strain at the location of DFOS can be
183 determined from the Brillouin frequency shift with temperature compensation as described by
184 Bao *et al.* (2015).

185 ***Thermocouple, Load and Displacement Sensors***

186 Each beam was instrumented with four glass-sheathed, K-type, bare-bead thermocouples (24
187 gage wire) peened into small (diameter < 2 mm) holes drilled into the bottom and top flanges as
188 indicated in Fig. 3: TC1 and TC3 at mid-span, and TC2 and TC4 at quarter-span. Additional
189 thermocouples were located throughout the test setup to characterize the test environment and
190 monitor safety-relevant temperatures. The thermocouples have a manufacturer-specified
191 temperature standard limit of error of 2.2°C or 0.75% (whichever value is greater) over a
192 measurement range of 0°C – 1250°C.

193 A calibrated (linearity: $\pm 0.03\%$, repeatability: $\pm 0.01\%$) load transducer by Omegadyn (LCR-
194 100), placed on a spanning bar at the bottom of the loading yoke, was used to measure the
195 applied load as illustrated in Figs. 1(a) and 1(c).

196 The mid-span vertical deflection at the bottom surface of the beam was measured using two
197 linear potentiometers (Novotechnik TR-0050) located below the burner rack and connected to
198 the beam via high-temperature ceramic fibers. The use of two fibers provided compensation for
199 the unwanted influence of gas temperature on displacement measurements with an estimated
200 expanded uncertainty of 0.2 mm (95% confidence).

201 **Test Protocol**

202 Each beam was subjected to both fire and mechanical loading. Fig. 4 illustrates the fire test
203 protocol. The heat release rate (HRR) was held approximately constant at five target levels: 25
204 kW, 65 kW, 120 kW, 195 kW, and 350 kW, which corresponded to beam temperatures at TC1 of

205 approximately 200°C, 400°C, 600°C, 850°C, and 1050°C, respectively. During the test of Beam
206 #2, the gas was turned off for about 20 seconds before the HRR was increased to 120 kW and
207 195 kW, respectively, to allow for visual observation. When the HRR was increased to a higher
208 level, the target value was overshoot and then quickly regulated down to the expected value. At
209 each HRR level, in addition to the self-weight, the beam was subjected to three levels of loads at
210 the mid-span. For Beam #1, the three loads were approximately 68 N, 98 N, and 126 N, and
211 sustained for 7 minutes, 4 minutes, and 4 minutes, respectively. For Beams #2 and #3, the three
212 loads were approximately 68 N, 176 N, and 285 N, each sustained for 6 minutes.

213 **THERMO-MECHANICAL ANALYSIS**

214 Traditionally, thermo-mechanical analysis of a structure subjected to fire is a multi-step
215 process that starts with prediction of the fire behavior. Distributions of heat flux to member
216 surfaces are calculated to provide boundary conditions to the thermo-mechanical analysis.
217 Temperature distributions in members are then determined by solving heat conduction equations
218 with the boundary conditions. Finally, the calculated temperature distributions are applied to
219 determine material properties, and thermally induced strain and the structural response can be
220 analyzed. This is a complex process and accumulated errors can be significant.

221 In this study, temperature distributions near the beam surface were directly measured with
222 the distributed fiber optic sensor (DFOS-T), eliminating the need for prediction of the thermal
223 boundary conditions. Researchers have previously investigated the relationship between the
224 temperatures on a beam surface and within the beam. A so-called “section factor” – the ratio of
225 the fire-exposed perimeter to the cross-sectional area – determines the heat transfer rate within
226 the beam. Larger section factors lead to higher heat transfer rates. When the section factor of an
227 unprotected steel section is larger than 300 m^{-1} , the temperature within steel can be considered to

228 be the same as the surface temperature (Li *et al.* 2006; Li and Wang 2012). Since the small test
229 beams (S3×5.7 section) had a section factor of 353 m^{-1} , the measured surface temperatures at the
230 top or bottom flange were approximately equal to those within the steel. Furthermore, due to the
231 small beam height, the vertical distributions of temperature over the beam height can be
232 approximated as linearly-distributed between the upper and lower surface temperatures (Choi
233 2008).

234 **High Temperature Steel Properties**

235 Temperature-dependent material properties governing structural behaviors include thermal,
236 mechanical, and deformation properties (Kodur *et al.* 2010). The thermal properties include
237 thermal conductivity, specific heat, and density. The mechanical properties include yield strength,
238 elastic modulus, and post-yielding stress-strain relationship. The deformation properties include
239 thermal expansion and creep.

240 Various models of temperature-dependent mechanical properties were compared by Li and
241 Wang (2012). In their study, four degradation laws of yield strength and elastic modulus of steel
242 at elevated temperatures and their corresponding thermal strains as shown in Fig. 5 were taken
243 from four standards: EN 1993-1-2 (ECS 2005), AS 4100 (SA 1998), CECS 200 (CECS 2006),
244 and ANSI/AISC 360-10 (AISC 2010). The reduction factors for yield strength and elastic
245 modulus are denoted by η_y and η_E , respectively. $\eta_y = f_{yT}/f_{y20}$, and $\eta_E = E_T/E_{20}$, where f_{y20} and f_{yT}
246 represent the yielding strengths at 20°C and arbitrary temperature T , respectively; E_{20} and E_T
247 represent the elastic moduli at 20°C and arbitrary temperature T , respectively.

248 **Mechanical Analysis**

249 With the measured temperature distributions and the temperature-dependent properties of the
250 steel, a finite element model of the beam was created using ABAQUS[®]. Three-dimensional 8-

251 node brick elements (2.5 mm mesh size) with reduced integration (C3D8R) were used to model
252 the simply-supported beam, as shown in Fig. 6. Based on the measured temperature distributions
253 and high temperature steel properties, user subroutines “UMAT” and “UTEMP” (SIMULIA
254 2014) were applied to define the temperature-dependent nonlinear plasticity of the steel and the
255 non-uniform temperature distributions, respectively.

256 **RESULTS AND DISCUSSION**

257 **Temperature Distributions**

258 Temperature distributions in steel Beam #2 are presented in Fig. 7 at the five investigated
259 HRR values ranging from 25 kW to 350 kW. At each HRR, the temperature distribution along
260 the beam was not symmetric about the mid-span. The overall temperature distribution pattern
261 varied as the HRR increased. These results generally agree with the visual observation that the
262 flames were somewhat asymmetrical during the tests. The asymmetry is attributed to variations
263 in the ventilation of the flame channel compartment and in the gas distribution among the four
264 burners. These results illustrate the complex behavior of fire that can cause predicted temperature
265 distributions to differ significantly from actual conditions (Cadorin and Franssen 2003;
266 McGrattan *et al.* 2010; Li and Zhang 2012).

267 Fig. 8 shows a representative temperature time history measured from TC1 in Beam #2. The
268 five plateaus corresponded to the five HRR levels in Fig. 4(a). At each sustained HRR level, the
269 beam temperature gradually stabilized to a temperature with some variation. The variations were
270 relatively small at low HRR values and became larger as the HRR was increased. To quantify the
271 temperature variations, the mean values and standard deviations were calculated over 15 minutes
272 for Beam #1, and 18 minutes for Beams #2 and #3 when the mechanical loads were applied at
273 each temperature level. The means and standard deviations are presented in Table 1. The

274 coefficient of variation for all the thermocouple readings is less than 3.6 %.

275 Similarly, to average out the effects of temperature fluctuation, five measurements were
276 made using the DFOS-T at each sustained temperature level. Each measurement was an implicit
277 average over 15 seconds to 40 seconds. The mean values and the standard deviations of five
278 measurements were calculated and compared with the thermocouple results listed in Table 1. The
279 DFOS-T readings have a maximum coefficient of variation of 4%, which was similar to that of
280 the thermocouples.

281 Table 1 also shows that the relative difference between the mean temperatures from the
282 DFOS-T and the thermocouple ranges from -10% to 8%. To understand the statistical
283 significance of the measurement differences, the average of mean temperature differences (four
284 for Beam #1, three for Beam #2, four for Beam #3) was calculated at each HRR level and
285 presented in Fig. 9 as an average temperature difference. In addition, the range of the mean
286 differences at 95% confidence level is represented by the error bar in Fig. 9. It can be observed
287 from Fig. 9 that the mean difference at 95% confidence level is less than 4.7%, which is
288 acceptable in most engineering applications. The discrepancies may be attributed to several
289 factors. First, the DFOS-T sensor was installed in a slightly different location than the
290 thermocouples. Second, the thermocouple beads were located slightly below the surface of the
291 beam and the DFOS-T slightly above the surface, and thus, the influence of gas temperature
292 variation on the measurements varied. Additionally, the thermocouples were not corrected for
293 radiation losses.

294 **Strains**

295 The simulated strains of Beam #2 under fire and 285 N loading using the mechanical
296 properties specified in the EN1993-1-2 code are presented in Fig. 10 for the first three HRR

297 levels. They include the effects of thermal elongation due to uniform temperature change,
298 thermal bending due to temperature gradient over the cross section, and mechanical bending due
299 to the applied load. At the applied load of 285 N, the mechanical bending caused elastic strain
300 only. Creep strain (time dependent) was not explicitly modeled in the thermo-mechanical
301 analysis, although creep was implicitly included in the stress-strain relationship and the
302 measured temperature distributions that were input into the model. Furthermore, the beam
303 changes its position with respect to the heat source when deflected significantly, altering the
304 temperature distribution in beam (Baum 2011). As deflection increases, the influence of
305 deflection on the temperature distribution was taken into account in thermal analysis through the
306 DFOS-T measurement.

307 The strains at the bottom flange and mid-span of Beam #2 due to thermal elongation, thermal
308 bending and mechanical bending are presented in Fig. 11 for the first three HRRs and all loading
309 conditions. Fig. 11 shows that the thermal elongation accounted for over 95% of thermal induced
310 strain, and the thermal strain accounted for over 95% of total strain. The observation that thermal
311 elongation effects dominated the response is supported by the fact that the top flange of the beam
312 is always subjected to positive strains as illustrated by Fig. 10.

313 The simulated strains are also compared in Fig. 11 with the strains measured by the
314 DFOS-ST1 sensors (average \pm one standard deviation of five readings). The variations of the
315 strain measurements – due mainly to temperature fluctuation – are small compared to their
316 average amplitudes. The simulated strains at HRR of 195 kW and 350 kW are not included in
317 Fig. 11 because the DFOS-ST sensors failed due to excessive fiber deformation. In general, the
318 simulated strains under the investigated heating and loading conditions compared well with their
319 corresponding measured strains. To quantify the difference, the strains simulated by finite

320 element analysis using the temperature-dependent properties specified in Fig. 5 and the measured
321 strains at the three DFOS-ST locations are compared under the highest load applied and HRR up
322 to 120 kW. Similar to Fig. 9, Fig. 12 shows the average of relative strain differences at the
323 DFOS-ST locations (three for each beam) at each HRR level, and the margin of error
324 (represented by the error bar) of the data for all beams at 95% confidence level. For the four
325 temperature-dependent material property models, the overall average strain difference ranges
326 from 9.7% (EN 1993-1-2) to 13% (CECS 200) at 95% confidence level. The EN 1993-1-2 code
327 gives the smallest margin of error.

328 The differences between the simulated and measured strains can be attributed to two main
329 physical phenomena. First, the temperature distribution selected in simulations from five
330 readings could be different from that at the moment of strain measurement. Second, the adopted
331 temperature-dependent properties in simulations may not accurately represent those of the test
332 beam. For example, the temperature-dependent properties suggested in the EN 1993-1-2 code
333 (ECS 2005) are based on the average values from a small number of steel types (Luecke *et al.*
334 2011). The second point can be further substantiated by the fact that the average strain
335 differences in Fig. 12 are mostly negative when the material properties specified in AS 4100
336 code are used since the thermal strain is the smallest as shown in Fig. 5(c).

337 **Mid-span Deflection**

338 Figs. 13(a) and (b) compare the simulated and the measured mid-span deflections for Beam
339 #1 and Beam #2 at all investigated HRRs and applied loads. Beam #3 is not reported because the
340 displacement sensor failed at the start of the test. The measurements from the displacement
341 sensors were corrected for the settlement of supports and thermal elongation of the sensor
342 attachments. The simulated mid-span deflection used the temperature-dependent material

343 properties specified in EN1993-1-2 (ECS 2005). Fig. 13 indicates that the simulated and
344 measured results are in good agreement up through 120 kW (about 600°C beam temperature).
345 The discrepancies at higher temperatures result primarily from not modeling creep. Additional
346 sources of error could come from a mismatch between the adopted temperature-dependent
347 properties and those of the test specimens as well as uncertainties in the displacement and fiber
348 optic sensor measurements. At elevated temperatures, the temperature-corrected displacement
349 measurements are within ± 0.2 mm of the manufacturer-specified accuracy of the linear
350 potentiometers.

351 According to the finite element analysis, 80% – 95% of mid-span deflection was due to
352 thermal bending when the HRR was at 120 kW. Since the thermal gradient of Beam #2 at HRR =
353 120 kW was smaller than that at HRR = 65 kW, the deflections at HRR = 120 kW were smaller
354 as indicated in Fig. 13(b). This seemingly surprising result suggests that the temperature
355 distribution in the beam largely depended on the fire dynamics and air circulation in our specific
356 test setup, and that prediction of structure response could be quite inaccurate of uniform heating
357 assumed. The significant difference in deflection trend between Beams #1 and #2 at HRR =
358 120 kW was likely due to the gas shutoff during the test of Beam #2.

359 At beam temperatures below 600°C (HRR < 120 kW in these tests), even the largest applied
360 load of 285 N was insufficient to cause significant deformation of the beam. This was a
361 limitation of the present tests. At beam temperatures above 600°C, the applied loads were
362 sufficient to cause extensive mechanical deformation through creep and allow for a more
363 differentiated assessment of thermal and mechanical contributions to beam response.

364 CONCLUSIONS

365 In this study, Brillouin scattering based fiber optic sensors were used to measure

366 temperatures and strains in steel beams exposed to fire. The measured temperatures along the top
367 and bottom flanges of the beams and their linearly interpolated temperatures in the webs of the
368 “I-shaped” sections were input to a finite element model of the beam with building code
369 specified temperature-dependent material properties. The following conclusions can be drawn
370 based on the experimental and computational results:

371 1 Distributed fiber optic temperature sensors can operate up to at least 1050°C in fire with
372 adequate sensitivity and accuracy for typical structural engineering applications. The
373 measured temperatures were validated by thermocouple measurements resulting in an
374 average relative difference of less than 4.7% at 95% confidence level.

375 2 When $HRR \leq 120$ kW, the maximum beam temperature was approximately 600°C. The
376 computational model provided an acceptable prediction of strains (average relative difference
377 < 13%) and mid-span deflections (0.31 mm maximum difference), when compared to direct
378 strain measurements by distributed fiber optic strain sensors and temperature compensated
379 potentiometers measurements, respectively. The material properties specified in EN 1993-1-2
380 resulted in the smallest margin of error among the four considered building codes. In our
381 tests, the thermal elongation (not thermal bending) accounted for over 95% of thermal strain,
382 and the thermal strain accounted for over 95% of total strain. At beam temperatures below
383 600°C, approximately 80% – 95% of mid-span deflection was due to the effects of thermal
384 bending.

385 3 When $HRR \geq 195$ kW, the mechanical loads had a greater influence on the mid-span
386 deflection due to substantial reduction of the mechanical properties of steel and the resulting
387 creep. Without explicitly considering creep effects in the simulations, the deformation was
388 significantly underestimated.

389 4 With a gage length factor of approximately 10, the distributed fiber optic strain sensors
390 captured large strains and maintained the fiber integrity until the beam temperatures reached
391 about 600°C. For large strain measurements at higher temperatures, a gage length factor of at
392 least 20 is suggested.

393 **ACKNOWLEDGEMENT**

394 This work was funded by the National Institute of Standards and Technology (NIST) under
395 Award No. 70NANB13H183. The contents of this paper reflect the views of the authors, and do
396 not necessarily reflect the official views or policies of NIST. Certain commercial equipment,
397 instruments, or materials are identified in this paper to specify the experimental procedure. Such
398 identification is not intended to imply recommendation or endorsement by NIST, nor to imply
399 the materials or equipment are necessarily the best available for the purpose.

400 **REFERENCES**

- 401 AISC. (2010). *Specifications for Structural Steel Buildings. ANSI/AISC 360-10*, American
402 Institute of Steel Construction, Chicago, IL.
- 403 AISC. (2011). *Steel Construction Manual, 14th edition*, American Institute of Steel Construction,
404 Chicago, IL.
- 405 Bao, X., and Chen, L. (2011). “Recent progress in Brillouin scattering based fiber sensors.” *Sens.*,
406 11, 4152-4187.
- 407 Bao, Y., and Chen, G. (2015). “Fully-distributed fiber optic sensor for strain measurement at
408 high temperature.” *Proc. 10th Int. Workshop Struct. Health. Monit.*, Stanford, CA.
- 409 Bao, Y., and Chen, G. (2016a). “Strain distribution and crack detection in thin unbonded
410 concrete pavement overlays with fully distributed fiber optic sensors.” *Opt. Eng.*, 55(1),
411 011008.

412 Bao, Y., and Chen, G. (2016b). "Temperature-dependent strain and temperature sensitivities of
413 fused silica single mode fiber sensors with pulse pre-pump Brillouin optical time domain
414 analysis." *Mes. Sci. Tech.*, under review.

415 Bao, Y., Meng, W., Chen, Y., Chen, G., and Khayat, K.H. (2015). "Measuring mortar shrinkage
416 and cracking by pulse pre-pump Brillouin optical time domain analysis with a single optical
417 fiber." *Mater. Lett.*, 145, 344-346.

418 Baum, H.R. (2011). "Simulating fire effects on complex building structures." *Mech. Res.*
419 *Commun.*, 38(1), 1-11.

420 Bertola, V., and Cafaro, E. (2009). "Deterministic-stochastic approach to compartment fire
421 modeling." *Proc. R. Soc. London, Ser. A*, 465, 1029-1041.

422 Bundy, M., Hamins, A., Johnsson, E.L., Kim, S.C., Ko, G.H., and Lenhart, D.B. (2007).
423 "Measurements of heat and combustion products in reduced-scale ventilation-limited
424 compartment fires." *NIST Technical Note 1483*.

425 Cadorin, J.F., and Franssen, J.M. (2003). "A tool to design steel elements submitted to
426 compartment fires OZone V2. Part 1: pre- and post-flashover compartment fire model." *Fire*
427 *Safety J.*, 38, 395-427.

428 CECS. (2006). *Technical Code for Fire Safety of Steel Structures in Buildings. CECS200-2006*,
429 China Association for Engineering Construction Standardization, China Plan Press.

430 Choi, J. (2008). "Concurrent fire dynamics models and thermomechanical analysis of steel and
431 concrete structures." PhD Dissertation submitted to the Graduate Faculty of Georgia Institute
432 of Technology, Atlanta, GA.

433 Dwaikat, M., Kodur, V., Quiel, S., and Garlock, M. (2011). "Experimental behavior of steel
434 beam-columns subjected to fire-induced thermal gradients." *J. Constr. Steel Res.*, 67(1), 30-

435 38.

436 ECS. (2005). *Eurocode 3: Design of Steel Structures - Part 1-2: General Rules - Structural Fire*
437 *Design. EN 1993-1-2*, European Committee for Standardization.

438 Huang, Z.F., and Tan, K.H. (2003). "Analytical fire resistance of axially restrained steel
439 columns." *J. Struct. Eng.*, 129(11), 1531-1537.

440 Huang, Y., Zhou, Z., Zhang, Y., Chen, G., and Xiao, H. (2010). "A temperature self-
441 compensated LPFG sensor for large strain measurements at high temperature." *IEEE Trans.*
442 *Instr. & Meas.*, 59(11), 2997-3004.

443 Huang, Y., Fang, X., Zhou, Z., Chen, G., and Xiao, H. (2013). "Large-strain optical fiber sensing
444 and real-time FEM updating of steel structures under the high temperature effect." *Smart*
445 *Mater. & Struct.*, 22(1), doi:10.1088/0964-1726/22/1/015016.

446 Jeffers, A.E., and Sotelino, E.D. (2012). "An efficient fiber element approach for the thermo-
447 structural simulation of non-uniformly heated frames." *Fire Safety J.*, 51, 18-26.

448 Kishida, K., and Li, C.H. (2006). "Pulse pre-pump-BOTDA technology for new generation of
449 distributed strain measuring system." *Proc. Struct. Health Monit of Intel. Infrastruct.*, 471-
450 477.

451 Kodur, V., Dwaikat, M., and Fike, R. (2010). "High-temperature properties of steel for fire
452 resistance modeling of structures." *J. Mater. Civ. Eng.*, 22(5), 423-434.

453 Kouzmina, I., Chien, C.K., Bell, P., and Fewkes, E. (2010). "Corning CPC protective coating –
454 an overview." *Report No. WP3703*, Corning Inc, USA.

455 Li, G., and Guo, S. (2008). "Experiment on restrained steel beams subjected to heating and
456 cooling." *J. Constr. Steel Res.*, 64(3), 268-274.

457 Li, G., Han, L., Lou, G., and Jiang, S. (2006). *Steel and Steel-concrete Composite Structures*

458 *Fire Resistance Design*. China Architecture and Building Press, (in Chinese).

459 Li, G. and Wang, P. (2012). *Advanced Analysis and Design for Fire Safety of Steel Structures*.
460 Zhejiang University Press, Hangzhou and Springer-Verlag Berlin Heidelberg.

461 Li, G., and Zhang, C. (2012). “Simple approach for calculating maximum temperature of
462 insulated steel members in natural-fires.” *J. Constr. Steel Res.*, 71, 104-110.

463 Luecke, W., Banovic, S., and McColskey, J. (2011) “High-temperature tensile constitutive data
464 and models for structural steels in fire.” *NIST Technical Note 1714*.

465 McGrattan, K., McDermott, R., Hostikka, S., and Floyd, J. (2010). “Fire dynamics simulator
466 (version 5) user's guide.” *NIST Special Publication 1019-5*.

467 McAllister, T., Luecke, W., Iadicola, M., Bundy, M. (2012) “Measurement of temperature,
468 displacement, and strain in structural components subject to fire effects: concepts and
469 candidate approaches.” *NIST Technical Note 1768*, 73.

470 Neubrex Co. Ltd. (2013). *User's Manual of Neubrescope NBX-7020*, Japan.

471 Sunder, S. S. et al. (2005). *Federal Building and Fire Safety Investigation of the World Trade*
472 *Center Disaster: Final Report of the National Construction Safety Team on the Collapses of*
473 *the World Trade Center Towers*. NIST NCSTAR 1, National Institute of Standards and
474 Technology, Gaithersburg, MD, 298.

475 Rinaudo, P., Torres, B., Paya-Zaforteza, I., Calderón, P.A., and Sales, S. (2015). “Evaluation of
476 new regenerated fiber Bragg grating high-temperature sensors in an ISO834 fire test.” *Fire*
477 *Safety J.*, 71, 332-339.

478 SA. (1998). *Steel Structures*. AS 4100-1998, Standards Association of Australian, Homebush,
479 NSW.

480 SIMULIA. (2014). *Abaqus User Subroutines Reference Manual Version 6.14*, Providence, RI,

481 USA.

482 Tan, K.H., Toh, W.S., Huang, Z.F., and Phng, G.H. (2007). "Structural responses of restrained
483 steel columns at elevated temperatures. Part 1: Experiments." *Eng. Struct.*, 29 (8), 1641-1652.

484 Usmani, A.S., Chung, Y.C., and Torero, J.L. (2003). "How did the WTC towers collapse: a new
485 theory." *Fire Safety J.*, 38(6), 501-533.

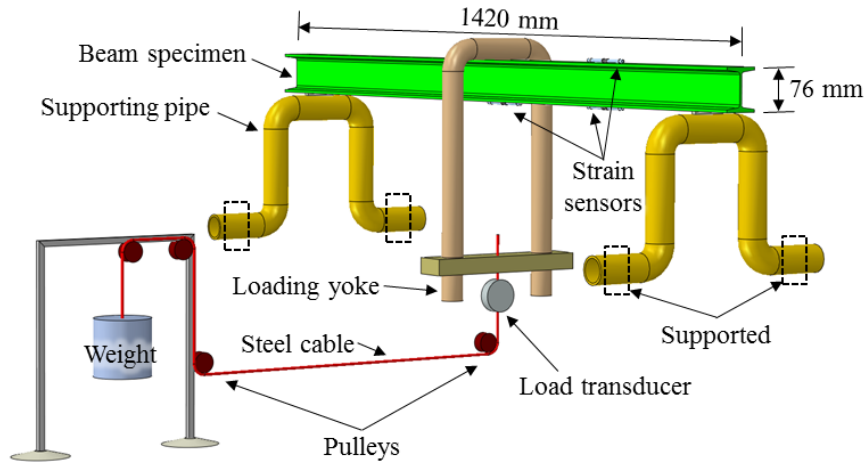
486 Usmani, A., Rotter, J. M., Lamont, S., and Gillie, M. (2001). "Fundamental principles of
487 structural behavior under thermal effects." *Fire Safety J.*, 36(8), 721-744.

488 Venugopalan, T., Sun, T., Grattan, K.T.V. (2010). "Temperature characterization of long period
489 gratings written in three different types of optical fibre for potential high temperature
490 measurements." *Sens. & Act. A: Phys.*, 160, 29-34.

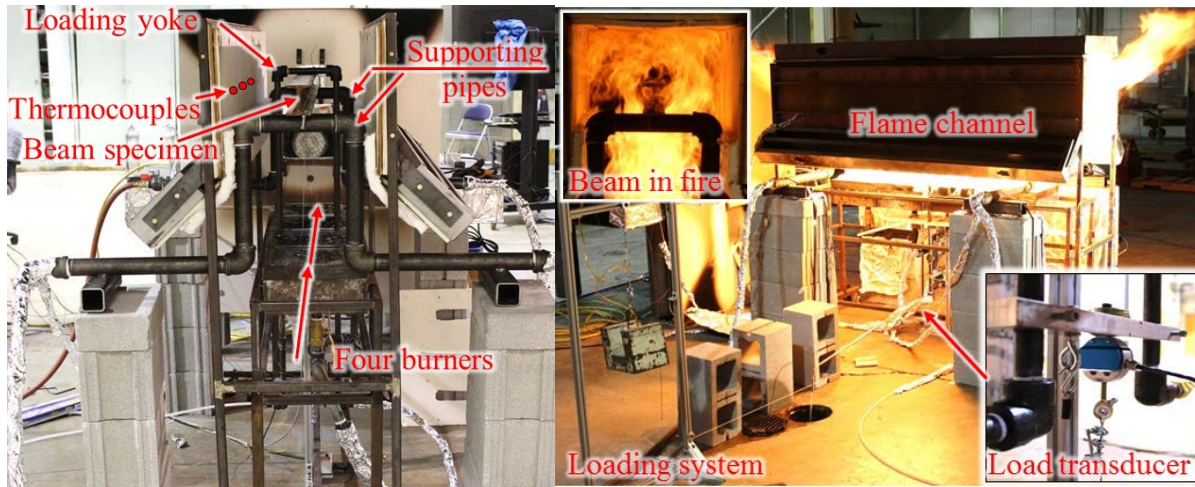
491 Zhang, B., and Kahrizi, M. (2007). "High-temperature resistance fiber Bragg grating temperature
492 sensor fabrication." *IEEE Sens. J.* 7, 586-591.

493 Zhang, C., Li, G., and Wang, Y. (2012). "Sensitivity study on using different formulae for
494 calculating the temperature of insulated steel members in natural fires." *Fire Technol.*, 48(2),
495 343-366.

496 Zhang, C., Gross, J., and McAllister, T. (2013). "Lateral torsional buckling of steel W-beams to
497 localized fires." *J. Constr. Steel Res.*, 88, 330-338.

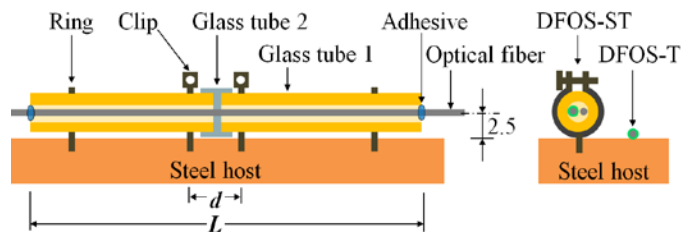


(a) Illustration of specimen loading system

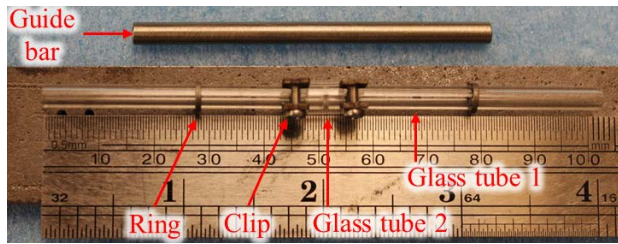


(b) Schematic of burners and specimen supports (c) Schematic of specimen loading system

Fig. 1. Test setup.



(a) Illustration (units in mm)



(b) Prototype attached to a steel substrate

Fig. 2. Fiber optic strain sensor.

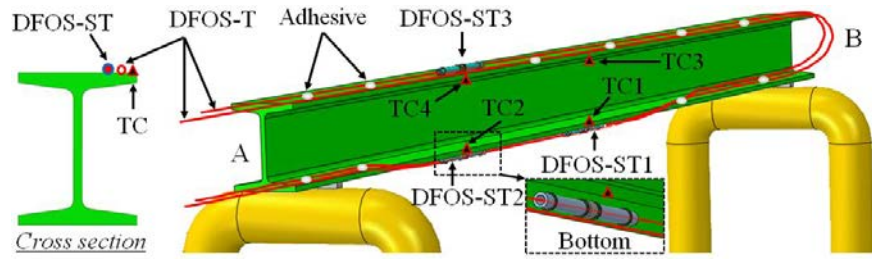


Fig. 3. Deployment of fiber optic sensors (DFOS-T, DFOS-ST) and thermocouples (TC).

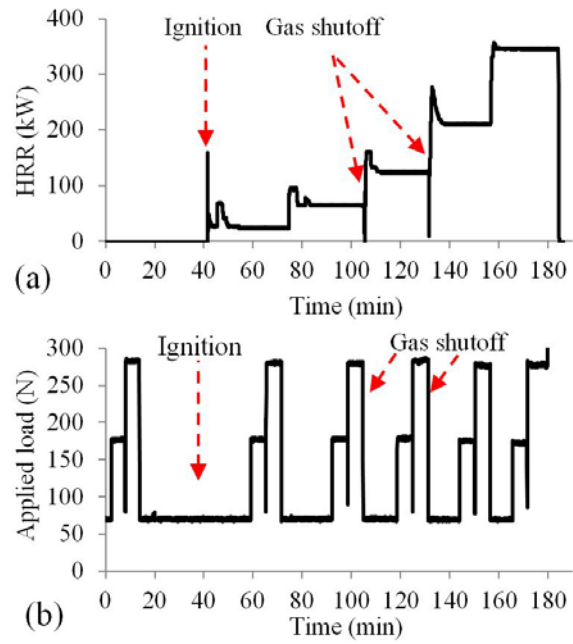
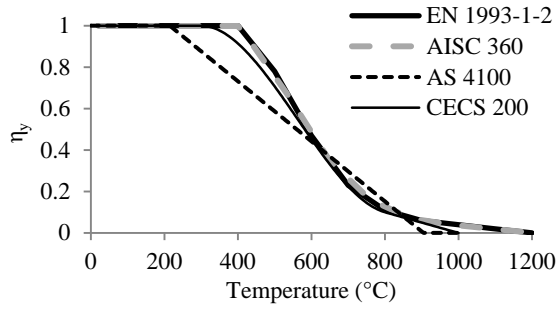
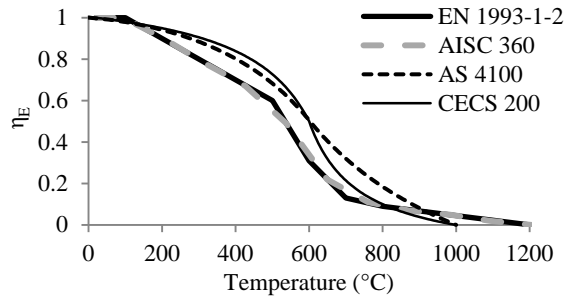


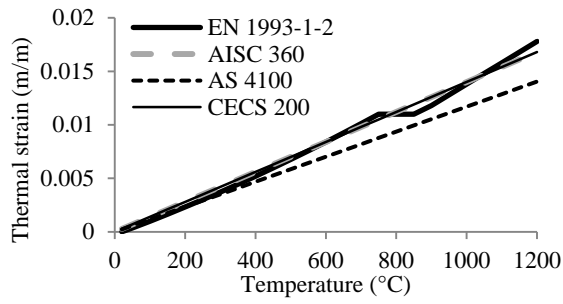
Fig. 4. Test protocols: (a) Heat Release Rate (HRR) versus time; (b) Applied load versus time.



(a) Yield strength



(b) Elastic modulus



(c) Thermal strain

Fig. 5. Comparison of material models.

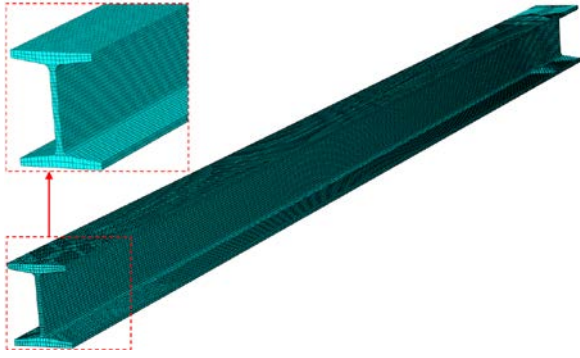
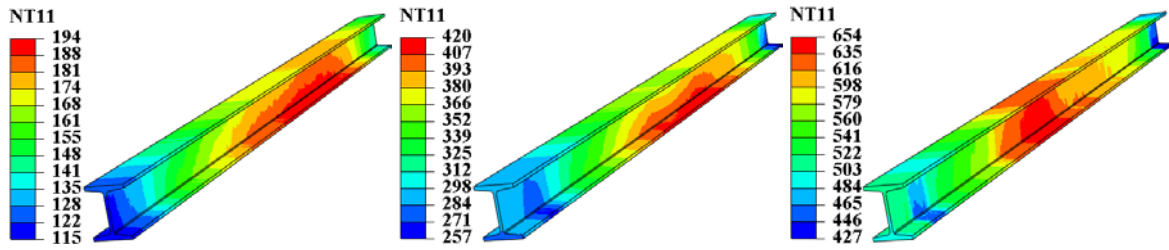


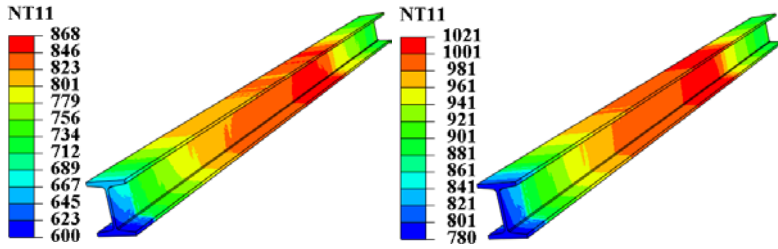
Fig. 6. Finite element model of steel beam specimen.



(a) HRR=25 kW

(b) HRR=65 kW

(c) HRR=120 kW



(d) HRR=195 kW

(e) HRR=350 kW

Fig. 7. Temperature distributions of Beam #2 at various heat release rates (HRR) measured using the DFOS-T sensor (temperatures in °C).

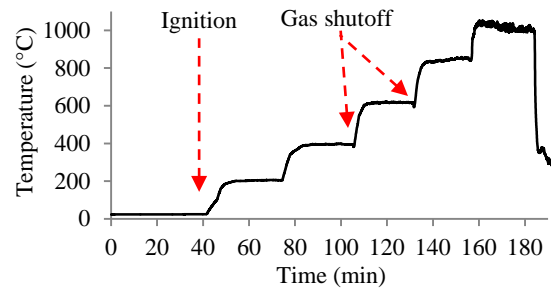


Fig. 8. Temperature time history measured by thermocouple TC1 in Beam #2.

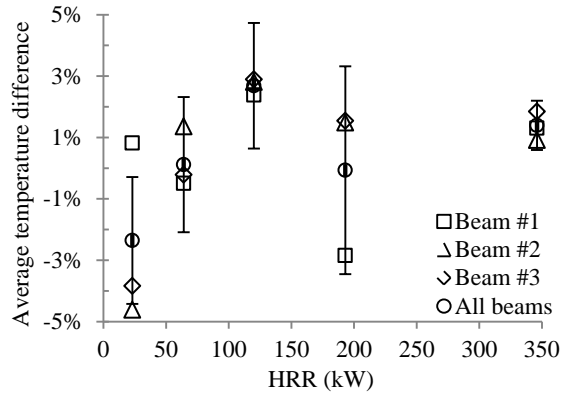


Fig. 9. Average relative difference between the fiber optic sensor (DFOS-T) and thermocouple (TC) temperature readings.

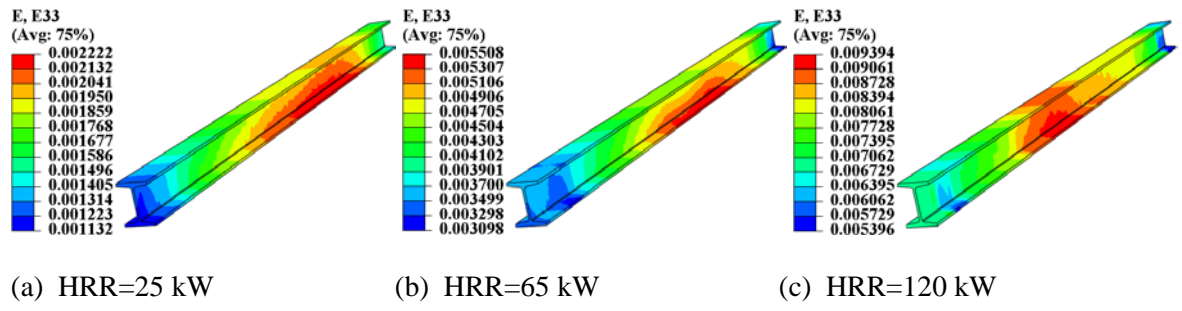
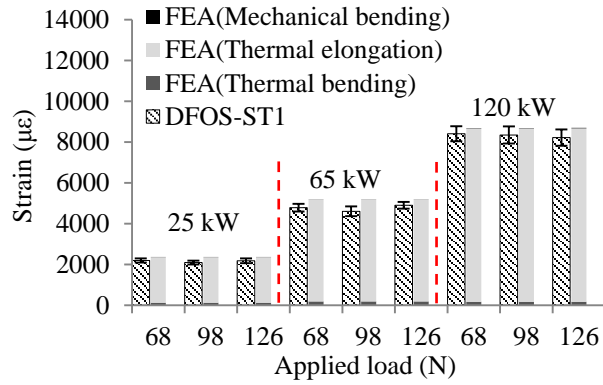
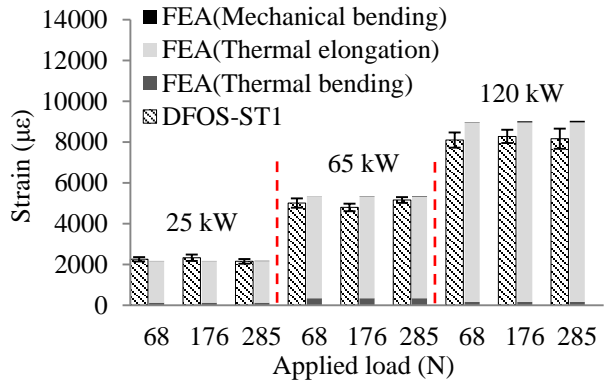


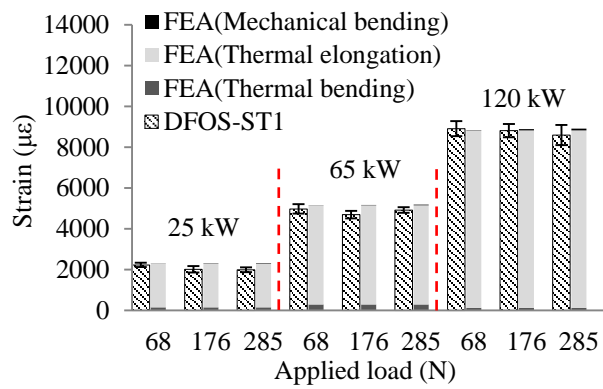
Fig. 10. Total strain distributions of Beam #2 under 285 N loading and fire.



(a) Beam #1



(b) Beam #2



(c) Beam #3

Fig. 11. Longitudinal strain on the bottom flange at mid-span of S3×5.7 steel beams under three point bending with a 1250 mm clear span.

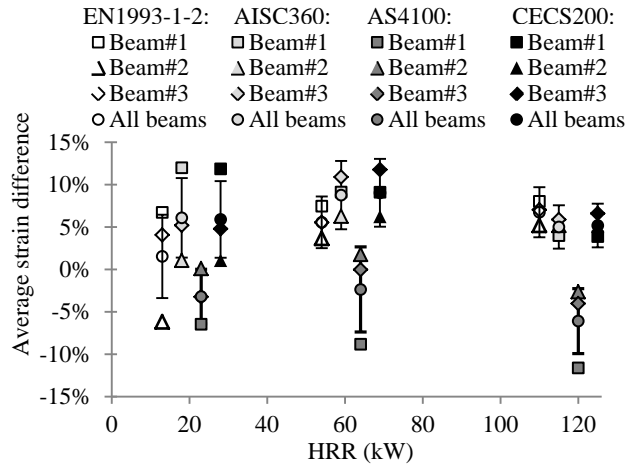
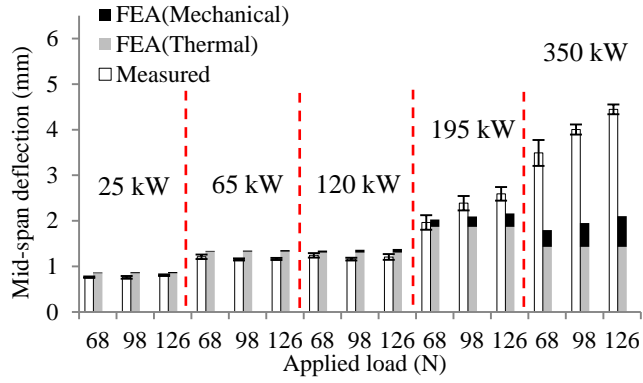
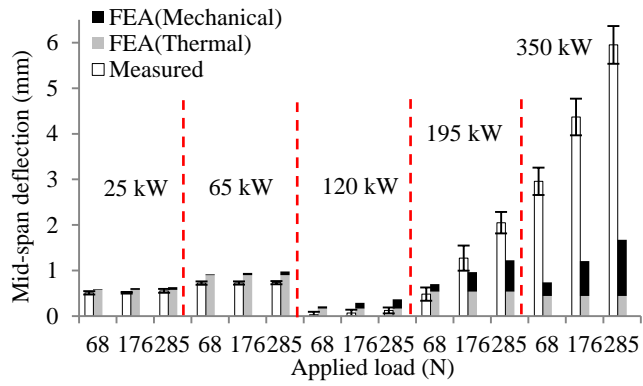


Fig. 12. Average relative difference between the simulated and measured strains under the highest load.



(a) Beam #1



(b) Beam #2

Fig. 13. Mid-span deflections of S3×5.7 steel beams under three point bending with a 1250 mm clear span.